Nuclear Instruments and Methods in Physics Research A 1061 (2024) 169107

Contents lists available at ScienceDirect

Nuclear Inst. and Methods in Physics Research, A

journal homepage: www.elsevier.com/locate/nima

Methods to maximize detector count rates on small-angle neutron scattering diffractometers at reactor sources: I. Optimizing wavelength selection

J.G. Barker *, J.C. Cook

NIST Center for Neutron Research, National Institute of Standards and Technology, 100 Bureau Dr, Gaithersburg, MD, 20899, USA

A R T I C L E I N F O

Keywords:
Neutron scattering
Small-angle scattering
Pinhole collimation
Wavelength optimization
Instrument resolution
Nuclear reactor

A B S T R A C T

Methods to determine the optimal neutron wavelength to maximize detector count rates on small angle neutron scattering (SANS) diffractometers at reactor sources is presented. Three experimental methods are used to determine the choice of optimal wavelength and collimation combination that maximizes the detector count rate. The wavelength optimization methods are applied to two different SANS diffractometers at the NCNR, and all methods are found to confirm the optimal wavelength of approximately 9.5 Å ± 0.5 Å for optically thin samples. The optimum wavelength is shifted by the wavelength-dependence of the sample transmission to 8.5 Å ± 0.5 Å for thicker absorbing samples or 6.5 Å ± 0.5 Å if the amount of multiple scattering needs to be minimized to limit scattering curve distortions. The same optimization methods can be applied to SANS diffractometers at other reactor facilities.

1. Introduction

Pinhole-type SANS diffractometers [1] measure the scattered radiation intensity as a function of momentum transfer, q, to characterize the fluctuations in scattering density in samples. The range and resolution of q required for a measurement depends upon the shape of the scattering intensity profile for the sample under study. The materials studied range widely from fluctuations in soft matter, such as microemulsions, polymer, and biological macromolecules, to features in hard materials such as alloys, ceramics, and magnetic systems. The typical diffractometer can measure a q-range that characterizes features from 1 nm to 100 nm in size, and it is key that high precision intensities are measured over this range. These intensities can vary by more than 10 orders in magnitude, with the lower bound limited by background scattering. Maximizing the incident intensity is important.

At reactor neutron sources, there are a variety of optical elements used to tailor the scattering experiment. Helical neutron velocity selectors (NVS) [2], by changing the rotation speed of the selector, are often used to choose a given mean neutron wavelength, λ, from the broad range of available values, typically 4 Å to 20 Å. The diffractometers themselves change the measured scattering angle θ by varying the source-to-sample apertures distance, L_1, by neutron guides insertion and by varying the sample-to-detector distance L_2, achieved by moving a two-dimensional (2-D) detector continuously on rails. Thus, the same momentum transfer q-range with the same q-resolution can be measured using several different combinations of wavelength and diffractometer distances and aperture sizes, and exploring the optimized wavelength setting is the purpose of this paper.

When compared to similar X-ray diffractometers, SANS diffractometers typically produce much lower count rates due to a much weaker radiation source. To increase the neutron count rates, the q-resolution is often relaxed allowing much broader wavelength distributions and less tightly collimated beams than found on X-ray diffractometers. In addition, the SANS diffractometers are physically quite large with count rates scaling roughly with the illuminated sample area. This paper explores how the choice of mean wavelength can be optimized to further increase the detector count rate. The second paper in this series explores optimization involving diffractometer lengths and aperture sizes [3].

SANS diffractometers typically have circular source and sample apertures having diameters D_1 and D_2, respectively, and a collimation geometry as shown in Fig. 1 Typically, a single 2-D detector is placed on rails to allow for continuous adjustability of the distance L_2 and the detection area is usually square with a pixel size Δ_D. The beam is blocked by a circular beam stop slightly larger than the beam diameter D_B placed

* Corresponding author.
E-mail address: john.barker@nist.gov (J.G. Barker).

https://doi.org/10.1016/j.nima.2024.169107
Received 6 September 2023; Received in revised form 3 January 2024; Accepted 12 January 2024
Available online 14 January 2024
0168-9002/Published by Elsevier B.V.

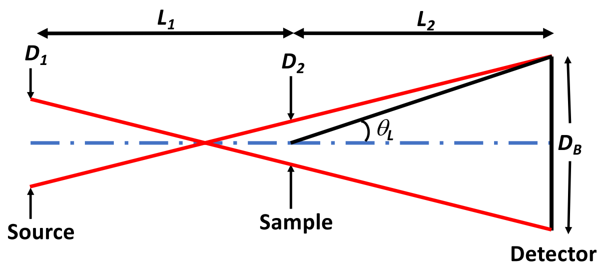

Fig. 1. Schematic of a pinhole SANS diffractometer's beam collimation.

just before the detector. The collimation distance, L_1, is changed in discrete steps by neutron guide element insertions downstream of the NVS.

For scattering with azimuthal symmetry, the 2-D detector data are radially-averaged where all pixels having a radial distance R with respect to the beam center in the range $R_i - \Delta_R/2 \le R \le R_i + \Delta_R/2$ are binned together in the same ith bin. The momentum transfer corresponding to this bin is

$$q_i = \frac{4\pi}{\lambda} sin(\theta_i / 2) \cong \frac{2\pi R_i}{\lambda L_2} \quad [1]$$

where θ_i is the scattering angle. For a sample of uniform thickness, the scattering probability and the intensity on the detector are proportional to the sample thickness and the detector count rate collected in the ith bin is

$$C_D(q_i) = \epsilon_D I_B d_s T_s \Delta\Omega_i \frac{d\Sigma}{d\Omega}(q_i) \quad [2]$$

where ε_D is the detector efficiency, d_s and T_s are the sample thickness and transmission, respectively, I_B is the beam current incident on the sample, $\Delta\Omega_i$ is the solid angle of the detector annulus, and $d\Sigma/d\Omega(q)$ is the macroscopic scattering cross-section of the sample. To minimize counting statistical errors, the goal is to maximize the detector count rate C_D collected over the same q-range $q_i - \Delta q/2 \le q \le q_i + \Delta q/2$ for a given sample. The solid angle collected within the ith annulus is then $\Delta\Omega_i \cong 2\pi R_i \Delta R/L_2^2 = \lambda^2 \Delta q q_i/2\pi$. The same q-range can be covered by the 2-D detector by varying L_1 and L_2 (inversely proportional to the wavelength λ) as long as the source and sample aperture diameters, D_1 and D_2 remain unchanged. Thus, we can set up the diffractometer in multiple equivalent configurations that cover an identical q-range with identical q-resolution simply by changing the wavelength λ and distances L_1 and L_2 in tandem. Falcao et al. [4] used similar measurements to optimize beam current under identical q-range and q-resolution conditions, but they studied optimizing both symmetric ($L_1 = L_2$) and asymmetric ($L_1 \neq L_2$) flight path geometries by keeping the wavelength λ, sample-to-detector distance L_2 and beam size D_B constant and changing only the source-to-sample distance L_1 and source and sample aperture sizes D_1 and D_2 in tandem.

The neutron source is relatively uniform in brightness across the area of the guide and divergence angle, so the beam current on the sample is given approximately by

$$I_B \cong \frac{A_1 A_2}{L_1^2} \Delta\lambda \epsilon_D T_G(L_1) P(\lambda) \quad [3]$$

where A_1 and A_2 are the source and sample aperture areas, $\Delta\lambda$ is the wavelength bandwidth passed by the NVS, $T_G(L_1)$ is a parameter that varies from 0 to 1 that accounts for guide transport losses caused by upstream gaps in the guide, and P is the moderator source brightness in units of $cm^{-2}s^{-1}sr^{-1}\text{Å}^{-1}$. T_G can be calculated using acceptance diagrams [5] and has been measured using Eq. (3) and found to vary between 0.8 and 1 for the diffractometers used in this study. After eliminating factors that do not depend upon wavelength, the detector count rate C_D can be related to both the beam current I_B and the observed source brightness P [6,7] as

$$\frac{C_D(q_i)}{d_S T_S} \propto \lambda^2 \epsilon_D I_B \propto \lambda^5 \epsilon_D T_G(L_1) P(\lambda) \quad [4]$$

Consequently, we have three independent experimental measures, C_D, I_B and $P(\lambda)$, to quantify wavelength dependence of the instrument performance.

A typical SANS diffractometer views a moderator around a neutron reactor source, with the neutrons transported along a neutron guide to the instrument. Often a localized cryogenically cooled moderator is placed within the view of the neutron guide, which shifts the spectrum $P(\lambda)$ to longer wavelengths producing a gain in brightness for cold neutrons. Ideally, the cryogenic moderator will shift the spectrum to follow a Maxwellian spectrum corresponding to the temperature of the moderator [8]. In practice the observed spectrum shape as seen by the instrument is distorted by the wavelength dependence of a number of factors: i) absorption cross-section proportional to wavelength within the moderator preferentially attenuating long wavelength neutrons, ii) neutrons leave the cold moderator without reaching thermal equilibrium, iii) instrument components, such as neutron windows and air paths, shift the wavelength spectrum by Bragg diffraction, absorption and other scattering processes, and iv) optical transmission losses from neutron guides produced by incomplete reflectivity or missing sections or cuts in the guide.

2. Wavelength optimization measurements

2.1. Beam brightness and guide losses

By removing the neutron velocity selector (NVS) from the beam and placing a chopper at the sample position to pulse the beam, the wavelength-dependent beam brightness $P(\lambda)$, as transmitted to the instrument's detector, can be directly measured by time-of-flight (TOF). For the VSANS diffractometer [9], the NVS is easily translated out of the beam. However, the factor of 5–10 increase in flux in the collimation section of such measurements requires prior attention to radiation safety issues that may result. In prohibitive cases, and for other SANS diffractometers where the NVS is not so easily removed, the beam brightness curve may be measured from the beam current I_B using Eq. (3) using a step-wise scan of the velocity selector wavelengths.

The NIST reactor, first generation liquid hydrogen (LH_2) cold source, and neutron guides are described in detail in Ref. [7], and for the second LH_2 cold source in Refs. [10,11]. The optical component design is largely described for the VSANS diffractometer by Ref. [9] and the NG-Bu 30m-SANS diffractometer by Refs. [7,11]. The main differences between the instruments are that the VSANS diffractometer uses a straight guide, NG-3, with a Be and Bi crystalline filter and the NG-Bu 30m-SANS diffractometer uses a curved guide, NG-Bu, for filtering.

For the NG-Bu 30m-SANS diffractometer, the beam brightness was measured via neutron time-of-flight (TOF) measurements prior to the instrument's installation [11]. The hydrogen cold source wavelength distribution was calculated from those same TOF measurements combined with simulations of the NG-Bu guide transmission. A similar procedure was used to measure the brightness curve $P(\lambda)$ on the VSANS instrument by placing a chopper at the sample position with signal recorded from the instrument's ^3He tube detectors 19.3 m downstream. This measurement was made with the cooled Be–Bi filter in the beam but with the NVS translated out of the beam. All nine guides were inserted. The pulse frequency was 16.67 s^{-1} with wavelength resolution 0.1 Å at full-width at half-maximum (fwhm). Fig. 2 shows the measured brightness, fit to the following expression, and scaled by λ^5 to be proportional to detector count rate, C_D/T_S, in Eq. (4).

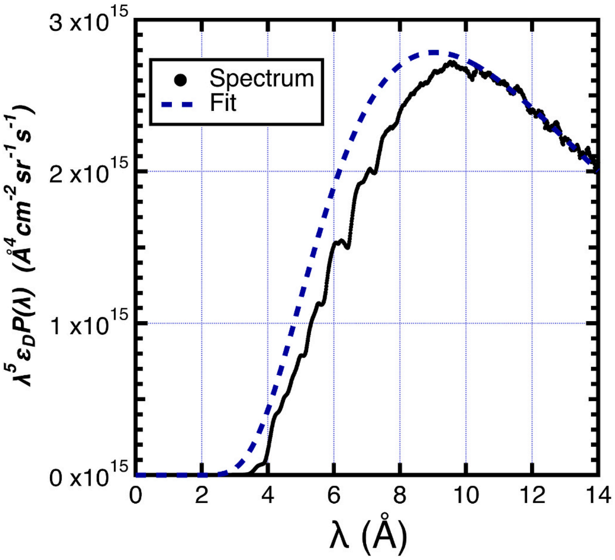

Fig. 2. The measured neutron time-of-flight (TOF) spectrum *P(λ)* (line) rescaled by wavelength to the fifth power for the VSANS diffractometer. The data is smoothed with a 20-point moving average for clarity. The standard error in the wavelength determination is 0.1 Å. Dashed curve represents a fit to *F(λ)* defined in Eq. (5) with fit parameter $A_L = 0.14$ Å^{-1} and fixed parameters $\lambda_T =$ 6.84 Å and $A_D = 0.365$ Å^{-1}.

$$\epsilon_D P(\lambda) \propto F(\lambda) \equiv \left(1 - e^{-A_D \lambda}\right) e^{-\lambda A_L} \frac{\lambda_T^4}{\lambda^5} e^{-\lambda_T^2/\lambda^2} \quad [5]$$

where the first term containing A_D accounts for the detector efficiency, the second term containing A_L represents attenuation processes and the third and fourth terms with λ_T represent a Maxwellian distribution with $\lambda_T = (949.3\ \mathrm{K\AA^2}/T_C)^{1/2} = 6.84$ Å, where $T_C = 20.3$ K at pressure of 0.1 MPa (1 bar) is the boiling temperature of liquid hydrogen. Note the potential long-wavelength ($\lambda \gg \lambda_T$) gain, G, from a cold moderator having temperature T_C over an ambient temperature moderator of temperature T_M, is $G \propto T_M^2/T_C^2$. The idealized gain for the NCNR cold source having an operating cold moderator temperature $T_C = 20.3$ K and heavy water moderator temperature $T_M = 320$ has $G \cong 250$, but the actual gain is somewhat less due to incomplete neutron moderation within the cold moderator and other attenuation losses. For example, at the Institut Laue-Langevin (ILL) in Grenoble, France, the measured cold moderator gain is 80–100 at $\lambda \geq 10$ Å [12]. We estimate the gain with the current cold moderator at the NCNR at long wavelengths to be around 50 to 60. The VSANS and 30m-SANS instruments' detector efficiencies have $A_D = 0.365$ Å^{-1} and 0.370 Å^{-1}, respectively. The VSANS data fit Eq. (5) best over the wavelength range 10 Å $\leq \lambda \leq$ 14 Å with $A_L = 0.14$ Å^{-1}. The measured curve peaks at a wavelength $\lambda \approx 9.7$ Å. The Be-filter removes most neutrons having wavelength $\lambda < 4$ Å by Bragg diffraction. Bragg scattering from large Bi grains a few cm in size also produce localized dips in the spectrum at $\lambda < 7.9$ Å, the Bragg cut-off for Bi. The guide transmission will be higher at longer wavelengths.

During guide transport parts of phase space at large beam divergence are preferentially lost. Often the dominant loss is caused by gaps in the guide path located between the moderator source and the source aperture and can be calculated using acceptance diagrams [5]. The largest gap is usually located at the velocity selector position. Losses caused by guide gaps are independent of wavelength but depend upon the beam divergence. Significant additional losses are often found to occur from guide section misalignment. Wavelength dependent losses can also occur whenever the beam divergence exceeds the critical angle of the mirror surface or from nonspecular scattering from supermirror surfaces.

The guide lost parameter T_G can be measured by taking the ratio of the beam current measured with instrument guides inserted and again without any guides where all possible ray paths collimated by the source and sample apertures avoid the guide gaps, and weighting both by the terms A_1, A_2, and L_1 in Eq. (3). Fig. 3a shows both the calculated and measured T_G for the VSANS diffractometer, with the lost limited to the range of 0.8–1.0. To check for possible guide misalignment, we routinely measure the guide loss parameter on all SANS diffractometers. Fig. 3b shows the variation in time. The combination of the translation motor vibrations and gravity is believed to drive the misalignment process of the vertical alignment screws with time. By adding a new locking mechanism to the alignment fixture in 2018, this recurring problem has now been resolved.

2.2. Fixed q-range methods

By choosing a series of instrument configurations that cover an identical q-range with the same q-resolution, we can compare both the beam current on the sample, I_B, and the count rate on the detector, C_D, obtained on test samples. The necessary choices made here are somewhat similar to what Falcao et al. [4] used to test beam optimization of collimation distances L_1 and L_2. For wavelength λ optimization, we fix the aperture diameters, D_1 and D_2, and the beam diameter, D_B. The ratio L_1/L_2 is also kept constant. For constant q, we then keep the quantity $L_1\lambda$ constant. Table 1 lists the available choices for L_1 for both diffractometers. With one guide, $N_G = 1$, inserted, the wavelength was set at $\lambda =$ 4.8 Å on the VSANS diffractometer and $\lambda = 3$ Å and 5 Å on the NG-Bu 30m-SANS diffractometer. The wavelengths were then scaled by η for each change in number of guides N_G and associated L_1 and L_2 distances as listed in Table 1. The q-range for the $\lambda = 5$ Å is shifted by a factor of 3/5 to smaller q than the $\lambda = 3$ Å data set, but the associated data set for either I_B or C_D can be rescaled vertically by a single value to place on a master curve.

Both diffractometers utilize rotating helical NVSs, which provide a triangular neutron velocity distribution with mean wavelengths over a broad range that depend on the rotational speed, and a fixed fwhm wavelength spread, $\Delta\lambda/\lambda$. On the VSANS instrument the available wavelength range is 4.5 Å $\leq \lambda \leq$ 9.2 Å and 12.7 Å $\leq \lambda \leq$ 19.3 Å with a spread $\Delta\lambda/\lambda = 12.5$ %. On the NG-Bu 30m-SANS diffractometer with the selector axis tilted to lower the resolution, the wavelength range is extended lower to 3 Å $\leq \lambda \leq$ 20 Å with a spread $\Delta\lambda/\lambda = 25.6$ %. Fig. 4a shows both the q-range and the standard deviation of the q-resolution σ_q

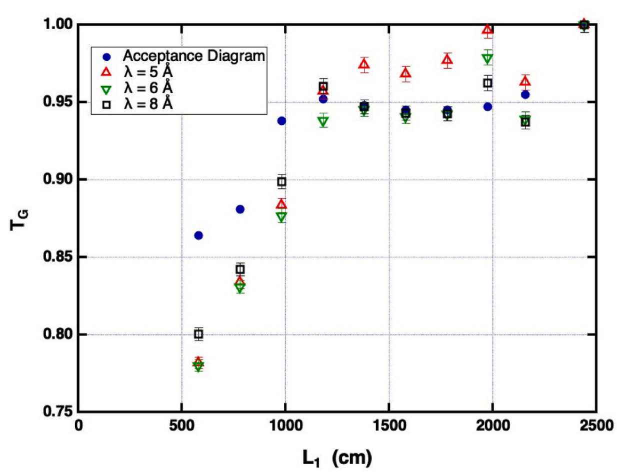

Fig. 3a. Measurement of guide losses T_G dependence with guide insertion on VSANS instrument as calculated from acceptance diagrams, and as measured at wavelengths of $\lambda = 5$ Å, 6 Å, and 8 Å.

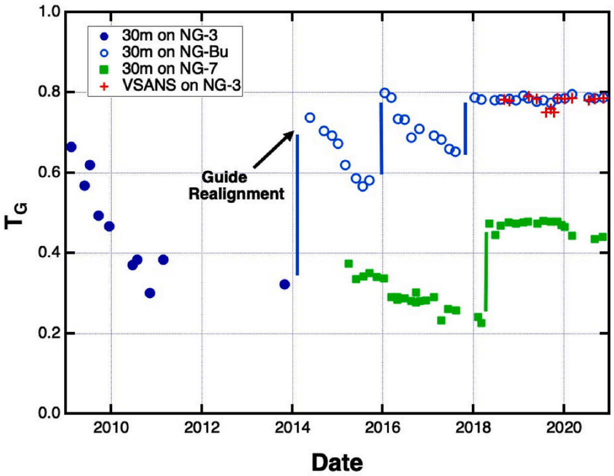

Fig. 3b. Variation with time of the guide losses T_G caused by guide misalignment. Measurements were made at $\lambda = 6$ Å for both 30 m SANS and the VSANS diffractometers with all guides inserted compared to with none inserted. Vertical lines indicate when the instrument's guides were realigned, restoring instrument performance. Ray tracing calculations predict $T_G = 0.64$ on guide NG-7 and 0.79 on guide NG-Bu for the 30 m SANS diffractometers.

Table 1
List of distances from source-to-sample apertures L_1 and sample-to-detector L_2 and ratio of wavelengths η depending upon number of guides N_G inserted (value of L_1) for both VSANS and NG-Bu 30m-SANS diffractometers measurements.

Diffractometer	VSANS	VSANS	VSANS	NG-Bu	NG-Bu	NG-Bu
N_G	L_1 (m)	L_2 (m)	$\eta=\lambda_N/\lambda_1$	L_1 (m)	L_2 (m)	$\eta=\lambda_N/\lambda_1$
1	21.37	20.06	1	14.72	13.17	1
2	19.56	18.36	1.09	13.17	11.78	1.12
3	17.62	16.53	1.21	11.62	10.40	1.27
4	15.62	14.65	1.37	10.07	9.01	1.46
5	13.61	12.77	1.57	8.52	7.02	1.73
6	11.61	10.89	1.84	6.97	6.24	2.11
7	9.60	9.00	2.20	5.42	4.85	2.72
8	7.60	7.12	2.82	3.87	3.46	3.80
9	5.59	5.23	3.83			

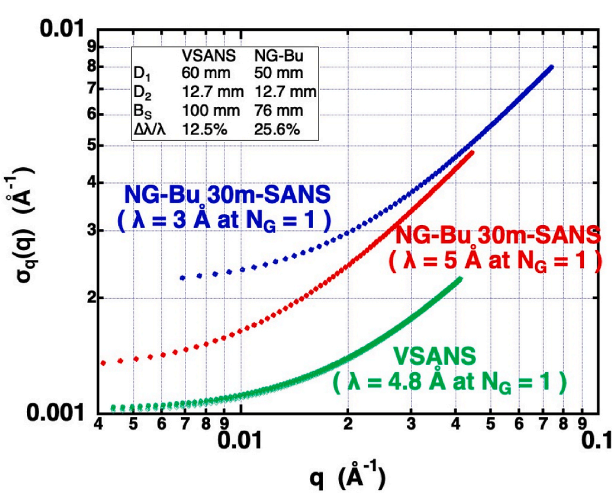

Fig. 4a. Plot of the q-resolution σ_q for all 24 instrument configurations listed in Table 1. Note that the q-resolution is nearly identical for each group of eight scaled configurations using the same color symbols, where $L_1 \propto L_2 \propto 1/\lambda$ is used to keep q-resolution nearly constant.

calculated using section 2 from Ref. [13], for the 24 different instrument configurations where three groups of eight configurations have nearly equivalent range and resolution.

The beam current, I_B, was measured for each instrument configuration directly using the 2-D detector by removing the beam stop and attenuating the beam with a variable thickness plastic attenuator. The count rates were then corrected for attenuation using a table of wavelength-dependent attenuation values. The scattering was measured from three strong scattering samples: poly tetrafluoroethylene (PTFE) that scatters primarily following a Porod law $I(q) \propto q^{-4}$, a porous silica sample having scattering that follows both a Porod law at smaller q which transitions to the Guinier law $I(q) \propto e^{-q^2 R_G^2}$ with a Guinier radius of $R_G = 33$ Å $\pm$ 1 Å at larger q, and a glassy carbon sample that scatters following a Guinier law with $R_G = 10$ Å $\pm$ 1 Å over the measured q-range. Fig. 4b plots the scattering results for the three samples for the eight instrument configurations taken on NG-Bu 30m-SANS starting at $\lambda = 5$ Å, which all overlap. The measured sample transmissions obtained by summing over the entire detector or over the area of the direct beam are plotted in Fig. 4c. The sample transmission using whole detector area was used in the data analysis since it mitigates multiple scattering scaling corrections [15], resulting in somewhat better overlap of the data sets in Fig. 4b. The glassy carbon sample showed the strongest wavelength dependence of T_S, which is dominated by multiple small-angle neutron scattering (MSANS). Multiple scattering can cause a change in the measured scattering curves, both in shape and vertical scale, as plotted in Fig. 4b. The change in scattering will also affect the measured detector count rate C_D in Eq. (2). If the measured sample transmission excludes the scattered signal, the measured scattering curves $d\Sigma/d\Omega(q)$ will be increased, sometimes quite significantly, over all values of q while if the transmission includes all the scattering signal the scattering curves will be decreased over all q [14,15]. By choosing to determine the sample transmission by summing over the entire detector, changes in the vertical scale of the scattering curves caused by multiple scattering are mitigated, but distortion in the shape of the curve remains. Samples that produce excessive multiple scattering should be avoided.

By choosing samples with very different scattering pattern shapes and strength of scattering, we tested whether the differences would affect the optimization results. Fig. 5a and Fig. 5b show the measurement results for the VSANS and NG-Bu 30m-SANS diffractometers, respectively. The detector count rate C_D is obtained by summing over the entire 2-D detector. Table 2 lists the parameters used to rescale the vertical scale to produce the best overlap of the data from the different

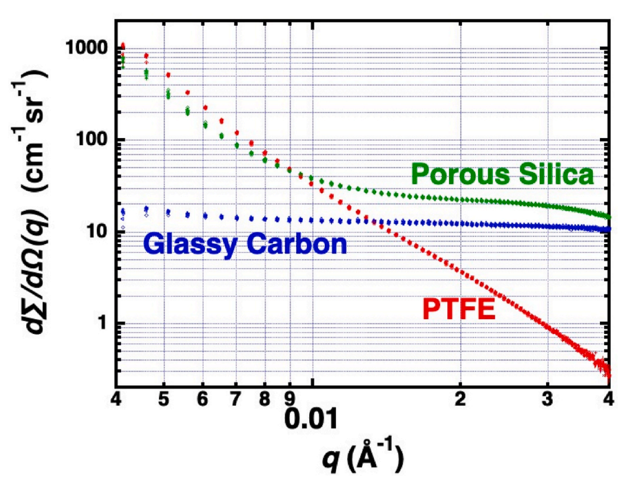

Fig. 4b. Plot of the scattering obtained on an absolute scale for the three samples measured. Plot contains eight separate measurements of each sample using eight different instrument configurations using NG-Bu 30m-SANS diffractometer with wavelength range 5.0 Å $\leq \lambda \leq$ 19.03 Å as listed in Table 1.

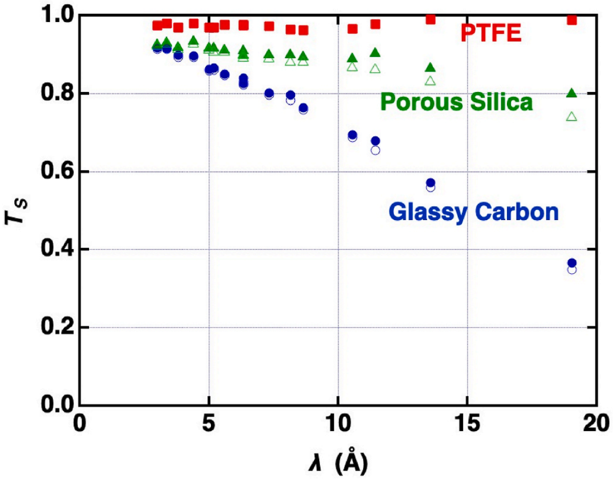

Fig. 4c. Plot of the measured sample transmission versus wavelength. Transmissions used in data reduction were determined by summing over the whole detector (solid symbols). For comparison purposes, transmissions determined by summing over a small area including only the direct beam are shown as open symbols.

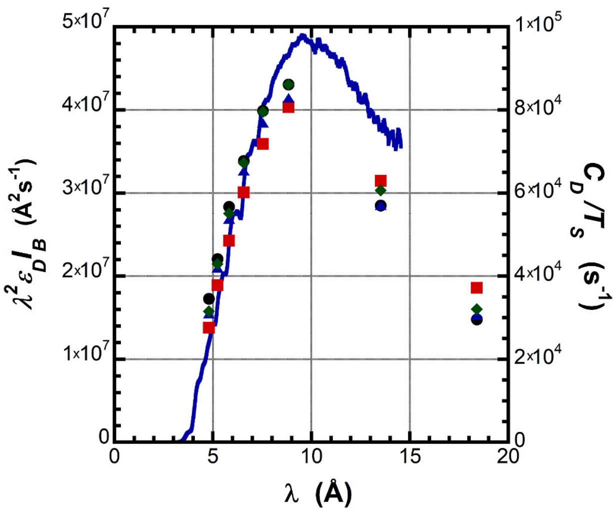

Fig. 5a. Plot combining the data from the three methods used to estimate the wavelength dependence of the detector C_D/T_S for a fixed q-range and q-resolution for the VSANS diffractometer: i) TOF spectrum (curve) $\lambda^5\varepsilon_D P(\lambda)$, ii) beam current $\lambda^2\varepsilon_D I_B$ (circles) and iii) 2-D detector count rates C_D/T_S summed over entire detector for PTFE (squares), 35 × glassy carbon (triangles) and 7 × porous silica (diamonds). After vertical rescaling, all three types of measurements show similar wavelength dependence.

samples and methods to produce a separate master curve for each instrument. The parameters account both for differences in the proportionalities found in Eq. (4), and to combine two different q-ranges in a single figure for instrument NG-Bu for Fig. 5b. The VSANS diffractometer's brightness curve appears to be shifted to slightly higher wavelength, by possibly 1 Å, but otherwise has the same general shape as the other methods. To double the number of points for the NG-Bu 30m-SANS diffractometer shown in Fig. 5b, the measurements were made at two different wavelengths in each instrument configuration requiring a separate vertical rescaling for each data set having equivalent q-range and as listed in Table 2. The data sets all overlap acceptably well with a peak performance near $\lambda = 9.0$ Å ± 0.5 Å.

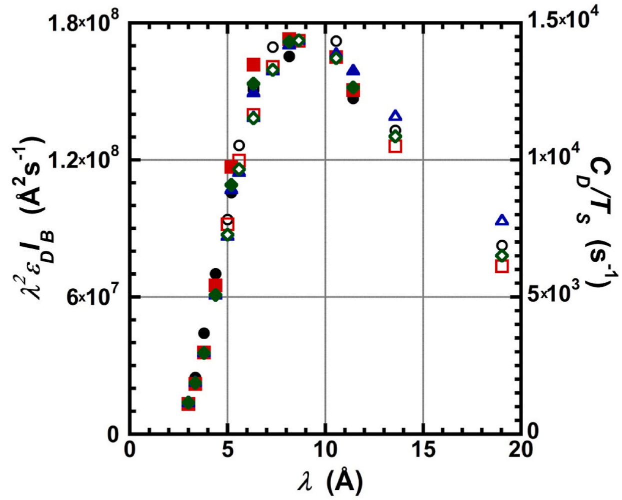

Fig. 5b. Plot of data taken on the NG-Bu 30m-SANS diffractometer combining two ways of estimating the wavelength dependence of the detector count rate: i) wavelength weighted beam current $\lambda^2 I_B$ (circles) and ii) detector count rates C_D/T summed over entire detector for PTFE (squares), glassy carbon (triangles) and porous silica (diamonds) samples. Closed and open symbols correspond to wavelengths scaled to one guide at 3 Å and 5 Å, respectively. After vertical rescaling, both types of measurements at two independent wavelengths show similar wavelength-dependence.

Table 2
List of parameters used to rescale data in Fig. 5a (VSANS) and Fig. 5b ($NG-B_u$) to overlay curves. The parameters account for both different scattering strength from the three different samples and for the two different sets of eight configurations covering different q-range on NG-Bu. The wavelength used with one guide inserted is labeled λ_1.

Instrument	λ_1	I_B	C_D (PTFE)	C_D (glassy carbon)	C_D porous carbon
VSANS	4.8 Å	1	1	35	7
NG-Bu	3.0 Å	1	1	0.31	0.21
NG-Bu	5.0 Å	2.6	1.15	1.92	0.74

3. Sample thickness and transmission considerations

To maximize the detector count rate C_D as shown in Fig. 5 we need to multiply by the sample thickness and transmission $d_S T_S$, which can alter the wavelength dependence. The transmission follows $T_S(\lambda) = e^{-d_S \Sigma_{tot}(\lambda)}$, where Σ_{tot} is the total macroscopic cross-section of sample. The quantity $d_S T_S$ is maximized when $d_S = 1/\Sigma_{tot}$. When the sample thickness chosen is much thinner than the ideal case such that $d_S \ll 1/\Sigma_{tot}$, or if the total cross-section Σ_{tot} is independent of wavelength, the optimization remains as represented in Fig. 5. But the neutron absorption cross-section varies as $\Sigma_a = B_a\lambda$, which dominates the total cross section in many magnetic or metallurgical materials. In soft matter studies, the solution is often composed primarily of either D_2O, H_2O, or other deuterated or hydrogenated organic solvents. To show the effect of the total cross-section Σ_{tot} on the optimization procedure, the measured brightness spectrum $\varepsilon_D P(\lambda)$ is multiplied by $1/(e\Sigma_{tot})$ for four representative materials: Fe, D_2O, H_2O and a sample exhibiting MSANS and is plotted in Fig. 6. The total cross section for Fe and H_2O can be approximated by linear terms: for Fe: $\Sigma_{tot} \cong \Sigma_a = B_a\lambda = 9.13 \times 10^{-3}$ Å^{-1}mm^{-1} × λ, and for H_2O: $\Sigma_{tot} \cong 0.412$ mm^{-1} + 0.039 Å^{-1}mm^{-1} × λ. For MSANS, the scattering follows $\Sigma_{tot} \propto \lambda^2$. The D_2O cross-section has a more complicated wavelength dependence and tabulated experimental values from Ref. [16] are used. For D_2O the peak position at $\lambda = 9.5$ Å ± 0.5 Å is not shifted noticeably since the minimum in the total cross-section, Σ_{tot},

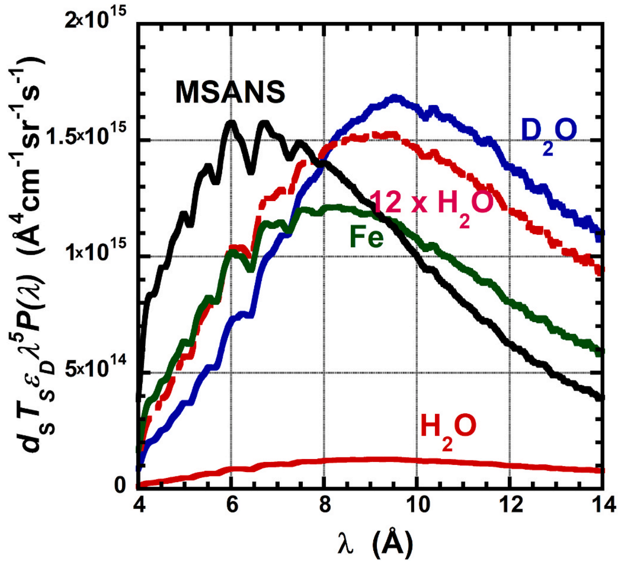

Fig. 6. The vertical scale is proportional to the predicted detector count rate C_D on the VSANS diffractometer for three representative materials: D_2O, H_2O, Fe ($B_a = 9.13 \times 10^{-3}$ $Å^{-1}mm^{-1}$), and samples whose scattering is dominated by MSANS. The sample thickness is chosen such that $d_S = 1/\Sigma_{tot}$. Note that for Fe, $\Sigma_{tot} \cong \Sigma_{abs} \propto \lambda$ and for MSANS $\Sigma_{tot} \cong \Sigma_{SAS} \propto \lambda^2$.

occurs near $\lambda = 9$ Å and the total cross section is relatively flat in the nearby region. The somewhat stronger wavelength-dependence in the H_2O cross-section shifts the peak to near $\lambda = 9.0$ Å $\pm$ 0.5 Å. Materials with substantial absorption cross sections, such as Fe, shift the peak to $\lambda = 8.5$ Å $\pm$ 0.5 Å. Materials that scatter strongly by MSANS, creates the largest shift of the peak to $\lambda = 6.5$ Å $\pm$ 0.5 Å

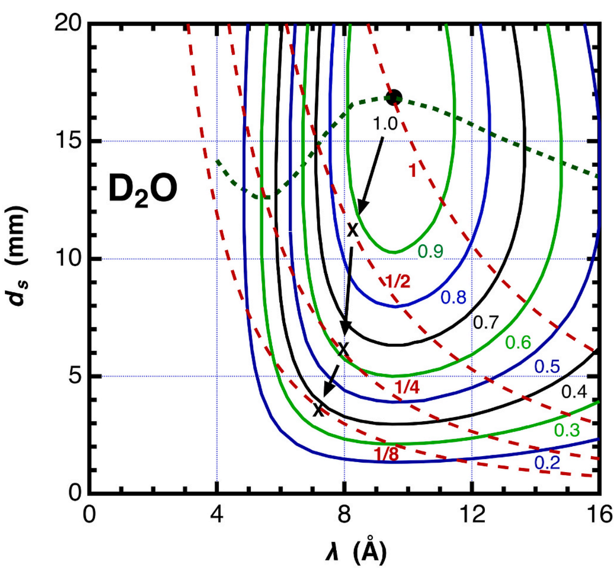

Fig. 7. Contour plots on the VSANS diffractometer of relative detector count rate versus wavelength, λ, and sample thickness, d_s, for samples containing D_2O solvent. Contour intensities are normalized to unity at the maximum represented by large circle. Short dash line corresponds to ideal sample transmission $T_S = 1/e$. Long-dash lines corresponds to constant scattering power $\sim d_s\lambda^2$. To reduce the amount of multiple scattering, follow a dashed curve having a lower fraction label (1/2, 1/4 or 1/8) to highest intensity contour which is marked with a X.

The effect of choosing both sample thickness, d_S, and wavelength, λ, away from the optimal conditions can be visualized in Fig. 7 for D_2O. The sample thickness is often chosen to be thinner than the optimal value: $d_S < 1/\Sigma_{tot}$ to either reduce the amount material needed if expensive or difficult to obtain, to minimize multiple scattering artefacts in the data, or to slightly improve the strength of the scattering signal above the flat incoherent background found in hydrogenated solvents.

The fraction of the scattering that scatters multiple times is proportional to the scattering power $\tau \propto d_S\lambda^2$. For introductory descriptions of the MSANS process see for example [14,15]. To minimize the amount of multiple scattering the sample thickness or wavelength can both be reduced. The dashed curves in Fig. 7 all represent conditions of constant scattering power τ with relative power labeled by factors of 2. The "X" symbols mark the position on the dashed curves where detector count rate is maximized. Note that the optimized path for reducing multiple scattering primarily proceeds by reducing the sample thickness first, and secondly by reducing the wavelength.

For samples where the SANS signal is weak when compared to the incoherent flat background, increasing the signal-to-noise (S/N) ratio often has a stronger improvement on data accuracy then the count rate. The background scattering obtained from liquid samples can sometimes be lowered by using samples thinner than the ideal $d_S = 1/\Sigma_{tot}$, where $T_S = 1/e$. For samples where the dominant background is from incoherent scattering, the thickness dependence of the background, or noise, can be estimated to follow [17].

$$\frac{d\Sigma_{inc}}{d\Omega}(q) \cong \frac{1}{4\pi}\frac{(1-T_{inc})}{d_s T_{inc}} \qquad [6]$$

where T_{inc} is the sample transmission dominated by incoherent scattering. By using a thinner sample, the background $d\Sigma_{inc}/d\Omega$ can be reduced somewhat. Multiple incoherent scattering also enhances the forward scattering by a further factor described in Ref. [18]. For example, by reducing the D_2O sample thickness d_S from the optimal 17 mm–5 mm, the background is reduced by a combined factor of 0.68 $\times$ 0.82 = 0.56. A similar improvement in the background can be made by reducing the H_2O sample thickness from the optimal 1.33 mm–0.4 mm.

Another consideration is the wavelength dependence of the background. Using Eq. (6), the wavelength dependence of the incoherent cross-section can also be estimated for both H_2O and D_2O. By changing the wavelength from 6 Å to 9 Å, the background for H_2O is calculated to increase by 24 %. But for D_2O is found to decrease by −26 %. Fortuitously, the local minima to the total cross-section for D_2O is near $\lambda = 9.5$ Å. Thus, considering both the wavelength and sample thickness dependence of the background, a higher S/N ratio will be achieved for H_2O using both a thickness of 0.5 mm and wavelength $\lambda = 6$ Å. After considering the wavelength dependence, the highest S/N is still obtained with D_2O at $\lambda = 9.5$ Å with sample thickness of 5 mm. For polycrystalline samples, double Bragg scattering background can be avoided by choosing a wavelength large enough to avoid Bragg scattering [18].

4. Conclusions

Three methods for determining the optimal wavelength to maximize detector count rates are presented. Instrument configurations are chosen such that the q-range covered by the 2-D detector is kept constant by having wavelength inversely proportional to instrument length: $\lambda \propto 1/L_1 \propto 1/L_2$. The three measures are i) measure detector count rate integrated over the entire 2-D detector, ii) measure the beam current I_B on sample weighted by λ^2, iii) measure beam brightness $\varepsilon_D P$ for all wavelengths simultaneously via TOF by removing the NVS weighted by λ^5. The chosen samples for the measurement should not scatter too strongly to avoid excessive multiple scattering, particularly at the longest wavelengths.

The observed optimal wavelength for both the VSANS and NG-Bu

30m-SANS diffractometers at the NCNR is found to be 9.5 Å ± 0.5 Å for thin samples, which is shifted to 8.5 Å ± 0.5 Å for thick absorbing samples having an ideal sample transmission $T_S = 1/e$. To mitigate scattering curve distortions caused by multiple scattering, the optimum wavelength is further shifted to 6.5 Å ± 0.5 Å for strong scattering samples. Differences in moderator, guide and detector designs at other SANS facilities will likely alter the shape of Fig. 5, and 6 and will require independent measurements. Most commonly SANS measurements at the NCNR have been done at a wavelength of 6 Å. By increasing the wavelength to the optimal choice, the count rate can be more than doubled for samples containing primarily D_2O solvent, increased by 50 % for H_2O solvent and by 25 % for samples dominated by absorption.

In cases where the scattering is weak when compared to the incoherent or other background sources, improving S/N can have a bigger impact on data accuracy then improving detector count rate. The optimum wavelength choice then may instead rely on background minimization.

CRediT authorship contribution statement

J.G. Barker: Writing – review & editing, Writing – original draft, Visualization, Validation, Methodology, Investigation, Formal analysis, Data curation, Conceptualization. **J.C. Cook:** Writing – review & editing, Formal analysis.

Declaration of competing interest

The authors declare the following financial interests/personal relationships which may be considered as potential competing interests:

John G Barker reports financial support was provided by National Institute of Standards and Technology. John G Barker reports financial support was provided by National Science Foundation.

Data availability

Data will be made available on request.

Acknowledgements

The authors express their thanks to Ryan Murphy, Charlie Glinka and Hubert King for critical reading and comments. The VSANS diffractometer is supported in part by the Center for High Resolution Neutron Scattering (CHRNS), a partnership between the National Institute of Standards and Technology and the National Science Foundation, under agreement No. DMR-2010792. All uncertainties in this paper represent one standard deviation.

References

[1] W. Schmatz, T. Springer, J. Schelten, K. Ibel, Neutron small-angle scattering: experimental techniques and applications, J. Appl. Crystallogr. 7 (1974) 96–116.
[2] L. Rosta, Neutron physical properties of a multidisc velocity selector, Physica B 156 (1989) 615–618.
[3] J.G. Barker, Methods to maximize detector count rates on small-angle neutron scattering diffractometers at reactor sources: II. Optimizing sample, source and detector sizes, Nucl. Instrum. Methods Phys. Res. 1016 (2023) 168973.
[4] A.N. Falcao, J.S. Pedersen, K. Mortensen, Optimum intensity in small-angle neutron scattering. An experimental comparison between symmetric and asymmetric geometries, J. Appl. Crystallogr. 27 (1994) 330–337.
[5] J.R.D. Copley, The joy of acceptance diagrams, J. Neutron Res. 1 (1993) 21–36.
[6] K. Ibel, The neutron small-angle camera D11 at the high-flux reactor, Grenoble, J. Appl. Crystallogr. 9 (1976) 296–309.
[7] C.J. Glinka, J.G. Barker, B. Hammouda, S. Krueger, J.J. Moyer, W.J. Orts, Small-angle neutron scattering instruments at the National Institute of standards and technology, J. Appl. Crystallogr. 31 (1998) 430–445.
[8] G.L. Squires, Introduction to the Theory of Thermal Neutron Scattering, Dover Publications, Inc., Mineola, New York, 1996.
[9] J.G. Barker, J.J. Moyer, S. Kline, G. Jensen, J.C. Cook, C. Gagnon, E. Kelley, J. P. Chabot, N. Maliszewskyj, C. Parikh, W. Chen, R.P. Murphy, C. Glinka, The very small angle neutron scattering instrument at the National Institute of Standards and technology, J. Appl. Crystallogr. 55 (2022) 271–283.
[10] R.E. Williams, J.M. Rowe, Developments in neutron beam devices and an advanced cold source for the NIST research reactor, Physica B 311 (2002) 117–122.
[11] J.C. Cook, J.G. Barker, J.M. Rowe, R.E. Williams, C. Gagnon, R.M. Lindstrom, R. M. Ibberson, D.A. Neumann, Experimental characterization of the advanced liquid hydrogen cold neutron source spectrum of the NBSR reactor at the NIST center for neutron research, Nucl. Instrum. Methods Phys. Res. 792 (2015) 15–27.
[12] P. Ageron, Cold neutron sources at ILL, Nucl. Instrum. Methods Phys. Res. 284 (1989) 197–199.
[13] J.G. Barker, J.S. Pedersen, Instrumental smearing effects in radially symmetric small-angle neutron scattering by numerical and analytical methods, J. Appl. Crystallogr. 28 (1995) 105–114.
[14] J. Schelten, W. Schmatz, Multiple-scattering treatment for small-angle scattering problems, J. Appl. Crystallogr. 13 (1980) 385–390.
[15] G.V. Jensen, J.G. Barker, Effects of multiple scattering encountered for various small-angle scattering model functions, J. Appl. Crystallogr. 51 (2018) 1455–1466.
[16] J.I. Marquez Damian, J.R. Granada, D.V. Baxter, S.R. Parnell, D.C. Evans, Measurement of the total cross section of heavy water in the 0.1 meV-1 eV energy range at 20 and 50 °C, Il Nuovo Cimento 38C (2015) 178.
[17] M. Shibayama, T. Matsunaga, M. Nagao, Evaluation of incoherent scattering intensity by transmission and sample thickness, J. Appl. Crystallogr. 42 (2009) 621–628.
[18] J.G. Barker, D.F.R. Mildner, Survey of background scattering from materials found in small-angle neutron scattering, J. Appl. Crystallogr. 48 (2015) 1055–1071.